AGU PUBLICATIONS

JGR

Journal of Geophysical Research: Space Physics

RESEARCH ARTICLE

10.1002/2014JA019798

Key Points:
- Ion acoustic solitary waves simulated by fluid and particle-in-cell simulations
- Fluid and PIC simulations show discrepancy in large-amplitude IASW features
- Kinetic treatment is required to model large-amplitude solitary waves

Correspondence to:
B. Kakad,
ebharati@iigs.iigm.res.in

Citation:
Kakad, B., A. Kakad, and Y. Omura (2014), Nonlinear evolution of ion acoustic solitary waves in space plasmas: Fluid and particle-in-cell simulations, *J. Geophys. Res. Space Physics*, *119*, doi:10.1002/2014JA019798.

Received 17 JAN 2014
Accepted 2 JUL 2014
Accepted article online 5 JUL 2014

Nonlinear evolution of ion acoustic solitary waves in space plasmas: Fluid and particle-in-cell simulations

Bharati Kakad[1], Amar Kakad[1,2], and Yoshiharu Omura[2]

[1]Indian Institute of Geomagnetism, New Mumbai, India, [2]Research Institute for Sustainable Humanosphere, Kyoto University, Kyoto, Japan

Abstract Spacecraft observations revealed the presence of electrostatic solitary waves (ESWs) in various regions of the Earth's magnetosphere. Over the years, many researchers have attempted to model these observations in terms of electron/ion acoustic solitary waves by using nonlinear fluid theory/simulations. The ESW structures predicted by fluid models can be inadequate due to its inability in handling kinetic effects. To provide clear view on the application of the fluid and kinetic treatments in modeling the ESWs, we perform both fluid and particle-in-cell (PIC) simulations of ion acoustic solitary waves (IASWs) and estimate the quantitative differences in their characteristics like speed, amplitude, and width. We find that the number of trapped electrons in the wave potential is higher for the IASW, which are generated by large-amplitude initial density perturbation (IDP). The present fluid and PIC simulation results are in close agreement for small amplitude IDPs, whereas for large IDPs they show discrepancy in the amplitude, width, and speed of the IASW, which is attributed to negligence of kinetic effects in the former approach. The speed of IASW in the fluid simulations increases with the increase of IASW amplitude, while the reverse tendency is seen in the PIC simulation. The present study suggests that the fluid treatment is appropriate when the magnitude of phase velocity of IASW is less than the ion acoustic (IA) speed obtained from their linear dispersion relation, whereas when it exceeds IA speed, it is necessary to include the kinetic effects in the model.

1. Introduction

Over the past three decades, many satellites (e.g., Polar, GEOTAIL, FAST, and Cluster) have observed the broadband electrostatic noise (BEN) in various regions of the Earth's magnetosphere [*Matsumoto et al.*, 1994; *Ergun et al.*, 1998; *Franz et al.*, 1998; *Bale et al.*, 1998; *Pickett et al.*, 2004]. From the GEOTAIL high time resolution plasma wave data, *Matsumoto et al.* [1994] showed for the first time that the broadband electrostatic noise emissions in the plasma sheet boundary layer are not a continuous noise but are composed of sequences of electrostatic impulsive solitary waves. Similar findings were confirmed later with the observations of electrostatic solitary waves (ESWs) in other boundary layer regions of the Earth's magnetosphere [*Ergun et al.*, 1998; *Franz et al.*, 1998; *Bale et al.*, 1998].

Two different models have been proposed for the generation mechanism of ESWs. One is a kinetic model, where electrons or ions are trapped by coherent potential structures in plasma [*Bernstein et al.*, 1957]. These solitary waves are called Bernstein-Greene-Kruskal (BGK) electron holes or ion holes because of their structures in the velocity phase space [*Matsumoto et al.*, 1994; *Omura et al.*, 1994, 1996; *Goldman et al.*, 1999; *Singh and Khazanov*, 2003]. The other is a nonlinear fluid model, where ESWs are electron or ion acoustic solitary waves/solitons that are generated due to the population of cold/hot electrons and ion fluids [*Dubouloz et al.*, 1993; *Berthomier et al.*, 1998; *Lakhina et al.*, 2009, 2011a, 2011b]. The fluid model employs either reductive perturbation technique [*Washimi and Taniuti*, 1966; *Dubouloz et al.*, 1993; *Kakad et al.*, 2009] or Sagdeev pseudo potential technique [*Sagdeev*, 1966; *Singh*, 1973; *Berthomier et al.*, 1998; *Singh et al.*, 2001; *Kakad et al.*, 2007; *Ghosh et al.*, 2008; *Lakhina et al.*, 2008a, 2008b, 2009; *Baluku et al.*, 2010; *Lakhina et al.*, 2011a, 2011b; *Verheest et al.*, 2013] to solve governing equations of plasma. The Mach number (soliton speed) range associated with the allowed solutions of the ion/electron acoustic solitons can be obtained using these techniques. However, these stationary soliton solutions do not provide information on their generation mechanisms and time evolutionary dynamics.

To address these issues, *Kakad et al.* [2013] performed fluid simulations to validate the nonlinear fluid theory of ion acoustic solitary wave (IASW). Their fluid simulation shows that the time evolution of short and long

wavelength initial density perturbation (IDP) evolve into two oppositely propagating identical ion acoustic solitons and soliton chains, respectively. The characteristics of the ion acoustic solitons during their stability are found to be the same as predicted by the nonlinear fluid theory.

The kinetic simulations of ESWs show that a significant amount of electrons/ions can be trapped inside the ESW potential. Such a behavior of electrons/ions affects the dynamics of ESWs. The fluid-based theories/simulations consider plasma constituents as fluids, which restrict the particle-trapping phenomenon in such models. Therefore, it is worthwhile to perform both fluid and particle simulations of ESWs to find the quantitative differences in the ESW characteristics obtained from each of them.

In this paper we perform fluid and particle simulations of IASW to investigate the effect of trapped electrons on the propagation characteristics of the IASW in plasmas. The fluid and particle simulation schemes are discussed in section 2. The characteristics of IASW obtained from the fluid and particle simulations are discussed in section 3. In section 4, we compare the results obtained from the fluid simulations with the particle simulations to address the differences in the IASW characteristics. We discuss the applicability of fluid and PIC approaches in the interpretation of IASW observations in the auroral region of Earth's magnetosphere in section 5.

2. Description of Simulation Models

2.1. One-Dimensional Fluid Code

We have developed a one-dimensional fluid code for homogeneous, collisionless two-component plasma consisting of fluid electrons and fluid ions (H^+ ions). For a nonlinear IASW propagating parallel to the magnetic field, the multifluid equations of continuity, momentum, and energy of each species and the Poisson equation govern the dynamic of the electrons and ions as follows:

$$\frac{\partial n_j}{\partial t} + \frac{\partial (n_j v_j)}{\partial x} = 0 \tag{1}$$

$$\frac{\partial v_j}{\partial t} + v_j \frac{\partial v_j}{\partial x} + \frac{1}{m_j n_j} \frac{\partial P_j}{\partial x} - \frac{Z_j}{m_j} E = 0 \tag{2}$$

$$\frac{\partial P_j}{\partial t} + v_j \frac{\partial P_j}{\partial x} + \gamma_j P_j \frac{\partial v_j}{\partial x} = 0 \tag{3}$$

$$\frac{\partial E}{\partial x} = (Z_i n_i + Z_e n_e)/\epsilon_0 \tag{4}$$

The electric field (E) in the equations listed above can be written in terms of an electrostatic potential (ϕ) with the relation, $E = -\partial\phi/\partial x$. The subscripts $j = e$ and i are respectively used for electrons and ions. The variables n_j, P_j, and v_j are plasma density, pressure, and velocity of the species j, respectively. Here m_j and Z_j respectively represent the mass and charge of the species j (i.e., $Z_e = -e$ for electrons and $Z_i = e$ for ions). ϵ_0 is the electric permittivity. We assume the adiabatic index $\gamma_e = 1$ for electrons and $\gamma_i = 3$ for ions in the equation of state given by equation (3). For a one-dimensional case, the allowed degree of freedom is 1, thus $\gamma_i = \gamma_e = 3$. However, we have taken $\gamma_e = 1$ in the present fluid simulation, as we propose the comparison of results retrieved from the fluid and PIC simulations. In the PIC simulation, it is noticed that the electrons are in thermal equilibrium for the ion acoustic mode. Hence, taking $\gamma_e = 1$ for the fluid simulation is appropriate approximation for its comparison with the PIC simulation. In the development of the fluid code, the above set of equations is solved by using numerical schemes that are discussed in *Kakad et al.* [2013].

2.2. One-Dimensional PIC Code

We have developed a one-dimensional electromagnetic PIC code based on the Kyoto university Electromagnetic Particle Code [*Omura and Matsumoto*, 1993]. In this code, Maxwell's equations and equations of motion are solved for a large number of superparticles [*Omura*, 2007]. Both spatial and time derivatives in the equations are solved by the centered difference scheme. We assume two species, electrons and ions, in the simulation system with the periodic boundary conditions. The initial velocity distributions of electrons and ions are assumed to be shifted-Maxwellian distributions given by

$$f_j(v) = \frac{n_j}{\sqrt{2\pi}\, V_{t\|j}} \exp\left(-\frac{(v - V_{d\|j})^2}{2V_{t\|j}^2} \right) \tag{5}$$

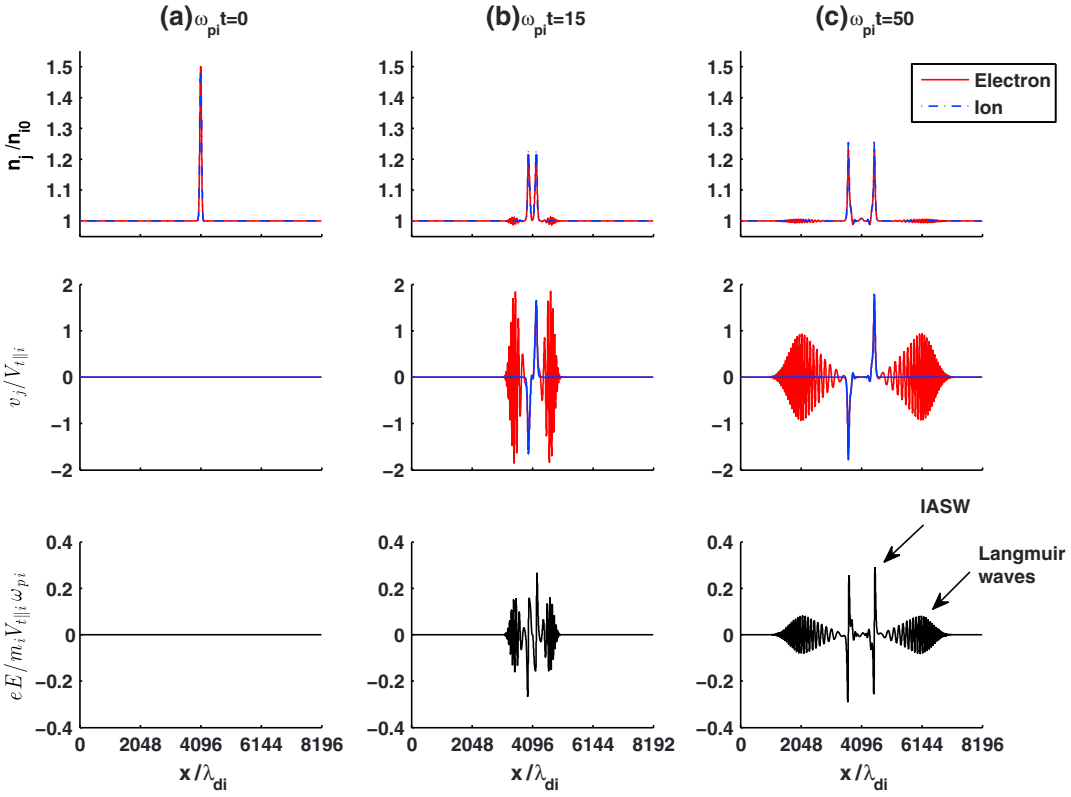

Figure 1. Snapshots of evolution of IASWs from fluid simulations. Initial densities and velocities of electrons and ions, and electric field are shown at (a) $\omega_{pi}t = 0$, (b) $\omega_{pi}t = 15$, and (c) $\omega_{pi}t = 50$.

where the subscripts $j = e$ and i represent the electrons and ions, respectively. The parameters $V_{t\|j}$, $V_{d\|j}$, and n_j represent the thermal velocity and drift velocity parallel to the magnetic field and number density for species j, respectively.

3. Simulation Results

3.1. One-Dimensional Fluid Simulation

We perform the fluid simulation in a one-dimensional system with the periodic boundary conditions. For all fluid simulation runs, we assume an artificial ion-to-electron mass ratio to be $m_i/m_e = 100$. The electron temperature considered is $T_e = 64T_i$. The flow velocities of electrons and ions are assumed to be zero initially, i.e., $v_{e0} = v_{i0} = 0$. The background electron and ion densities are set to one, i.e., $n_{e0} = n_{i0} = n_0$ and $\omega_{pe} = 10\omega_{pi}$. These background densities are superimposed by a localized Gaussian type perturbation of the following form:

$$\delta n = \Delta n \exp\left(-\frac{(x - x_c)^2}{l_0^2}\right) \tag{6}$$

In the equation above, Δn and l_0 gives the amplitude and width of superimposed density perturbation. Here x_c is the center of the simulation system. Thus, the perturbed densities $n_j(x) = n_{j0} + \delta n$ takes the following form as the initial condition:

$$n_j(x) = n_{j0} + \Delta n \exp\left(-\frac{(x - x_c)^2}{l_0^2}\right) \tag{7}$$

We perform four simulation runs with different density perturbations $\Delta n = 0.05$ (Run-1), 0.1 (Run-2), 0.2 (Run-3), and 0.5 (Run-4). We take grid spacing $\Delta x = 1\lambda_{di}$, time interval $\Delta t = 0.001\omega_{pi}^{-1}$, system length $L_x = 8192\lambda_{di}$, and $l_0 = 40.96\lambda_{di}$ for all fluid simulation runs. Here we discuss the generation and evolution of the IASW for Run-4 ($\Delta n = 0.5$) in detail. In Figure 1, we show some of the selected snapshots of the

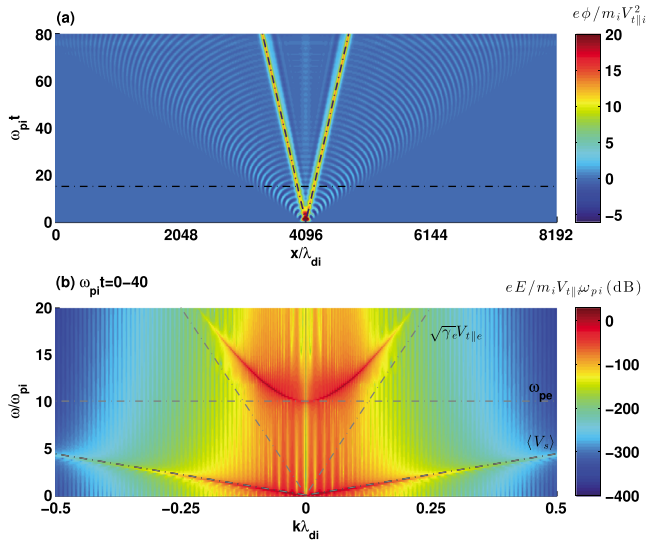

Figure 2. (a) Spatial and temporal evolution of electrostatic potentials for the fluid simulation with $l_0 = 40.96\lambda_{di}$, $\Delta n = 0.5$ (Run-4). The dark red bands correspond to IASWs that are propagating opposite of each other. The distinct wave structures, seen ahead of IASWs represents Langmuir wave. (b) ω-k dispersion diagrams during $\omega_{pi}t$ = 0–40 for Run-4. It shows presence of both Langmuir and ion acoustic mode. The speed of Langmuir mode (IA mode) estimated from their standard linear dispersion equation(spatiotemporal propagation) is shown with the slanted dash-dotted lines. The speed of ion acoustic mode obtained from linear dispersion is $V_{IA} = 8.18V_{t\|i}$. The electron plasma frequency is shown with horizontal black dash-dotted line at $\omega = 10\omega_{pi}$.

electron and ion densities (n_e, n_i), velocities (v_e, v_i), and electric field (E) associated with the IASW at different time stages of the fluid simulation. In this figure, Figure 1a shows n_e, n_i, v_e, v_i, and E at $\omega_{pi}t = 0$, when the background densities were superimposed by the localized perturbation. Here t is a product of the number of simulation time steps and Δt. It is observed that the IDP evolves into two identical IASWs along with the Langmuir waves at $\omega_{pi}t = 15$. In Figure 1b, the two bipolar electric field pulses represent the IASWs, whereas the two wave packets ahead of each IASW are the Langmuir oscillations. The bipolar electric field pulses at $\omega_{pi}t = 15$ are unstable, which later become stable when the Langmuir wave packets are detached from the solitary pulses [*Kakad et al.*, 2013]. One such snap of a considerably stable IASW at $\omega_{pi}t = 50$ are shown in Figure 1c. We examine the evolution and propagation of different wave structures through spatial and temporal evolution of their electrostatic potential (ϕ), which is depicted in Figure 2a. Here $x = 4096\lambda_{di}$ represents the center of the simulation system. The horizontal dash-dotted line shown in Figure 2a at $\omega_{pi}t = 15$ corresponds to the time of the formation of two unstable IASWs. After their formation, these IASWs propagate opposite to each other and it is seen as two slanted red bands. The distinct wave structures ahead of both red bands represent the propagation of Langmuir waves. The presence of the ion acoustic and Langmuir modes are confirmed through dispersion diagram. The ω-k diagram obtained by Fourier transforming the electric field in space and time for periods $\omega_{pi}t$ = 0–40 is shown in Figure 2b. The lower dispersion curves are for ion acoustic modes, whereas the dispersion curves starting at $\omega = 10\omega_{pi}$ corresponds to the Langmuir modes. The average speed of ion acoustic mode obtained from its spatial and temporal variations and the speed of Langmuir mode obtained from its linear dispersion relation (i.e., $\sqrt{\gamma_e}V_{t\|e}$) are shown by slanted dash-dotted lines in Figure 2b. The group velocity of the Langmuir waves is found to be greater than $\sqrt{\gamma_e}V_{t\|e}$, where $V_{t\|e} = \sqrt{T_e/m_e}$ is electron thermal speed, which is in accordance with their linear dispersion relation. It is noted that the average propagation speed $\langle V_s\rangle$ of the IASW is in agreement with the magnitude of phase velocity ($V_{IA} = 8.18V_{t\|i}$) obtained from the linear dispersion relation of the ion acoustic mode.

The average amplitude, width, and speed of the IASW estimated during $\omega_{pi}t$ = 40–80 are given in Table 1. It is noticed that the average amplitude of the IASW $e\langle\phi_m\rangle/m_iV_{t\|i}^2 = 12.96 \pm 0.08$. As the standard error

Table 1. Average Characteristics of IASW From Fluid and PIC Simulations During $\omega_{pi}t$ = 40–80

		Fluid Simulation			PIC Simulation		
Run	Δn	ϕ ($m_iV_{t\|i}^2/e$)	Width (λ_{di})	V_s ($V_{t\|i}$)	ϕ ($m_iV_{t\|i}^2/e$)	Width (λ_{di})	V_s ($V_{t\|i}$)
1	0.05	1.28 ± 0.04	88.4 ± 4.62	8.00 ± 0.06	1.20 ± 0.12	92.80 ± 14.2	8.00 ± 0.62
2	0.1	2.48 ± 0.08	85.8 ± 3.68	8.04 ± 0.06	2.32 ± 0.16	84.02 ± 8.36	7.70 ± 0.52
3	0.2	5.04 ± 0.12	79.6 ± 2.44	8.22 ± 0.04	3.99 ± 0.52	74.24 ± 11.5	7.32 ± 0.24
4	0.5	12.96 ± 0.08	61.6 ± 1.20	8.78 ± 0.04	8.48 ± 0.88	57.66 ± 4.52	7.16 ± 0.18

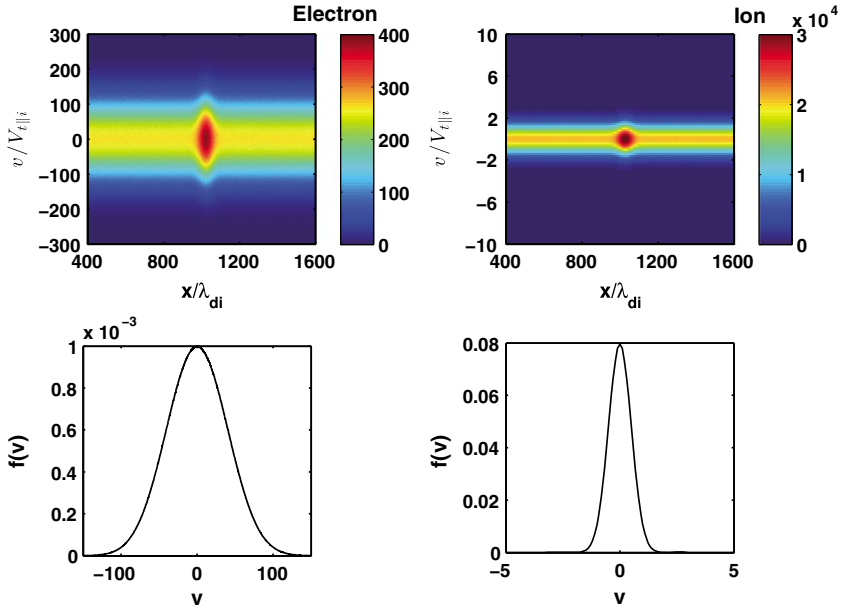

Figure 3. (top row) Distribution of electron and ion in *x*-*v* space and (bottom row) corresponding $f(v)$ as a function of v.

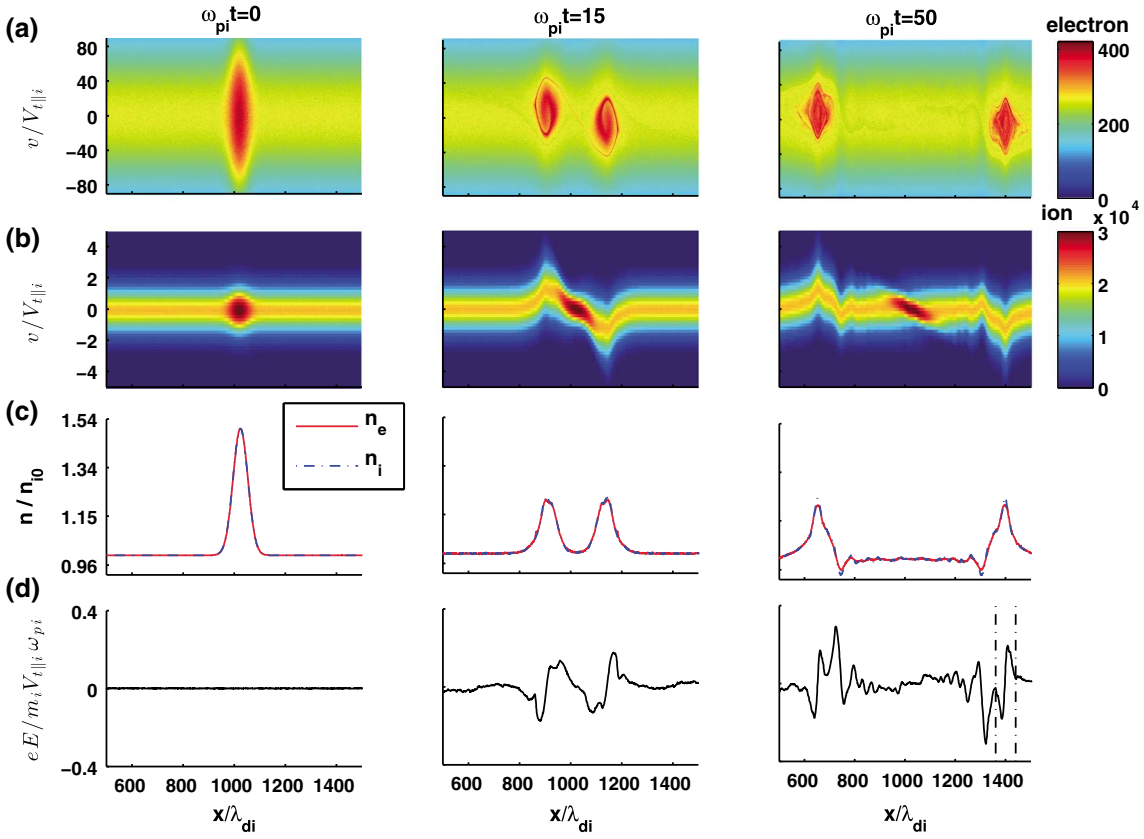

Figure 4. Distribution of (a) electrons and (b) ions in *x*-*v* space, (c) number density of electrons and ions, and (d) electric field as a function of x at $\omega_{pi}t = 0$, $\omega_{pi}t = 15$, and $\omega_{pi}t = 50$ are shown for $\Delta n = 0.5$ (PIC Run-4).

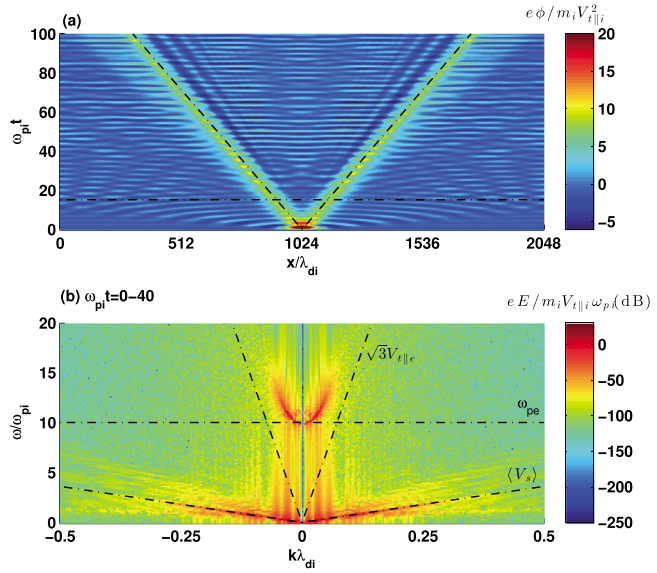

Figure 5. (a) Spatial and temporal evolution of electrostatic potentials for the PIC simulation with $l_0 = 40.96\lambda_{di}$, $\Delta n = 0.5$ (Run-4). The dark yellow bands correspond to the positive potential associated with the electron vortices propagating in opposite direction. (b) ω-k dispersion diagrams during $\omega_{pi}t = 0$–40 for Run-4. It shows the presence of both Langmuir and ion acoustic modes. The speeds of Langmuir mode and IA mode estimated respectively from their standard linear dispersion and spatial-temporal variations are shown with the slanted dash-dotted lines. The electron plasma frequency is shown with the horizontal black dash-dotted line at $\omega = 10\omega_{pi}$.

in the average amplitude of the IASW is ~0.6%, they are assumed to be considerably stable during their propagation from $\omega_{pi}t = 40$–80. Similar estimates are obtained for Run-1, Run-2, and Run-3 that are given in Table 1. It is noted that the average amplitude and speed of the IASW increase with the amplitude of IDP, whereas the average width of the IASW decreases.

3.2. One-Dimensional PIC Simulation

We perform the PIC simulation in the one-dimensional system with the periodic boundary conditions. The parameters for all PIC simulation runs are grid spacing $\Delta x = 1\lambda_{di}$, time interval $\Delta t = 0.001\omega_{pi}^{-1}$, system length $L_x = 2048\lambda_{di}$, mass ratio $m_i/m_e = 100$, thermal velocities $V_{t\|e} = 80V_{t\|i}$, drift velocities $V_{d\|e} = V_{d\|i} = 0$, and plasma frequencies $\omega_{pe} = 10\omega_{pi}$. The values of $V_{t\|e}$ and $V_{t\|i}$ imply that $T_e = 64T_i$. Like the fluid simulation, in PIC simulation the superparticles are distributed as described by equation (7). We take 2.75×10^5 superparticles per cell on average that corresponds to 5.63×10^8 superparticles in the simulation system for each species. It is emphasized that the idea of using large number of particles in the PIC simulation is to reduce thermal fluctuations which disturb coherent wave structures. This allows us to compare the IASW characteristics of the PIC simulation with those of the fluid simulation more accurately.

Using the PIC code we have taken four simulation runs for $\Delta n = 0.05$, 0.1, 0.2, and 0.5 and $l_0 = 40.96\lambda_{di}$. Here we discuss the simulation run with $\Delta n = 0.5$. Figure 3 (top row) shows the x-v phase space plots of electrons and ions at $\omega_{pi}t = 0$, when the IDP is introduced in uniformly distributed superparticles. The corresponding distribution functions $f_e(v)$ for the electrons and $f_i(v)$ for ions are shown in Figure 3 (bottom row).

The evolution of the IASW is shown by x-v phase diagrams of the electrons and ions in Figures 4a and 4b, respectively. The left, middle, and third columns of Figure 4 show parameters at $\omega_{pi}t = 0$, 15, and 50, respectively. The corresponding distributions of electron and ion superparticles, and the electric field are shown in Figures 4c and 4d, respectively. It is found that the IDP evolves in two vortices of trapped electrons at $\omega_{pi}t = 15$. In these vortices the population of trapped electrons is greater than the density of free and reflected particles. The ions are also found to respond to the motion of electrons and, as a result, two humps are seen in the ion distribution. The electron vortices and the displacement of the ions are responsible for the generation of two indistinguishable bipolar electric field pulses of the IASW. After their formation, these two electron vortices propagate toward the simulation boundaries in a direction opposite to each other with the average speed $\langle V_s \rangle$.

The spatial and temporal evolution of electrostatic potentials associated with different modes is illustrated in Figure 5a. The horizontal dotted line at $\omega_{pi}t = 15$ indicates the time of formation of two electron vortices. Dark yellow slanted bands seen in this figure indicate the propagation paths of two positive potential structures associated with these electron vortices in the x-t domain. Thus, the slopes of these bands give the propagation speeds of the IASW as shown by black dashed lines in Figure 5a. Here the Langmuir wave structures are not distinctly seen unlike fluid simulations. However, the presence of these modes is confirmed by

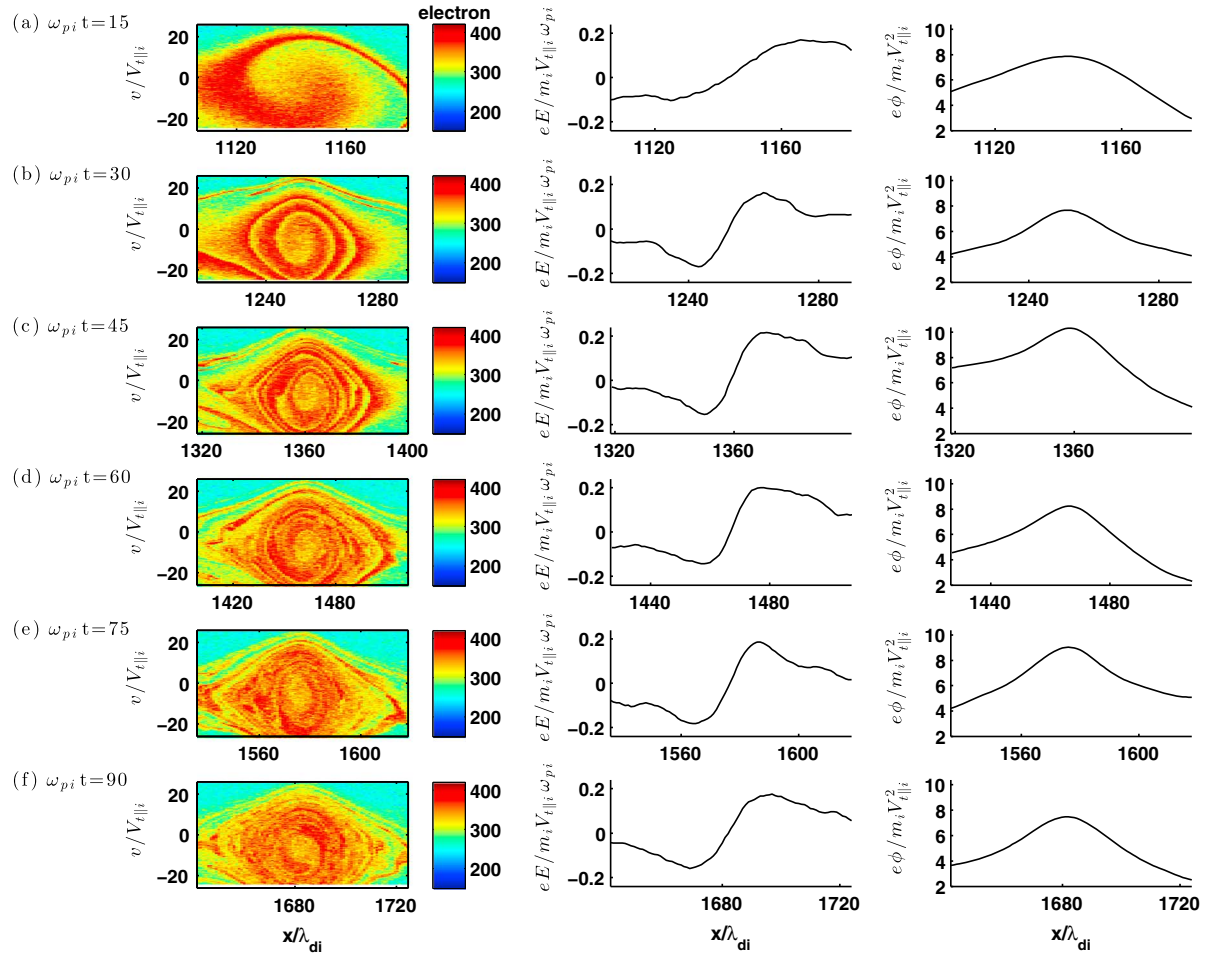

Figure 6. (a) Distribution of electrons in *x*-*v*, (b) corresponding electric field, and (c) potential for electron vortex propagating toward right-side boundary of the simulation system are shown at different time stages of the PIC simulation Run-4.

the ω-k diagrams shown in Figure 5b. This dispersion plot is obtained by Fourier transforming the electric field in space and time for a period of $\omega_{pi}t$ = 0–40. It shows the presence of both ion acoustic and Langmuir modes. Two lower dispersion curves in Figure 5(b) indicate the ion acoustic mode, whereas the upper dispersion curves that start at $\omega = 10\omega_{pi}$ represent the Langmuir modes. The speed of the ion acoustic mode obtained from its spatial and temporal variations and the speed of the Langmuir mode obtained from its linear dispersion relation are shown by slanted black dash-dotted lines in this figure. It should be noted that the behavior of electrons are different for both ion acoustic and Langmuir modes. The speed of ion acoustic mode obtained from their spatial-temporal propagation is in accordance with the phase speed obtained from its linear dispersion relation by taking $\gamma_e = 1$. Thus, we conclude that the electrons behave as if they are in thermal equilibrium for ion acoustic mode. However, the electrons are not found to be at thermal equilibrium for the Langmuir mode, as the upper dispersion curves in Figure 5b give the group velocity close to $\sqrt{3}V_{t\|e}$ for this mode. We calculate the average amplitude, speed, and width of IASW linked with the electron vortices during $\omega_{pi}t$ = 40–80. For $\Delta n = 0.5$, these estimates are found to be $e\langle\phi_m\rangle/m_iV_{t\|i}^2 = 8.48 \pm 0.88$, $\langle V_s\rangle/V_{t\|i} = 7.16 \pm 0.18$, and $\langle width\rangle/\lambda_{di} = 57.66 \pm 4.52$. The PIC data for Run-1, Run-2, and Run-3 are also analyzed, and the average estimates of these parameters are given in Table 1.

It is found that the amplitude and speed of the IASW linked with the electron vortices decrease rapidly after their formation. These structures are not stable as their characteristics change due to the electron trapping process. The snapshots of the electron vortex propagating toward the positive boundary of the simulation system are shown in Figures 6a–6f with the *x*-*v* phase plot for different time stages of the simulation Run-4. The corresponding electric field and potential are also shown in the same figure. It is observed that

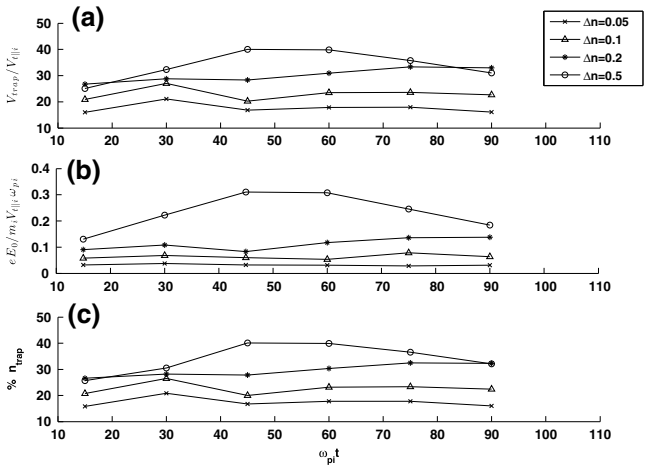

Figure 7. (a) Trapping velocity, (b) peak electric field, and (c) percentage of electrons trapped by the IASW potential linked with the electron vortex propagating toward the right-side boundary of the simulation system is shown as a function of time for the PIC simulation Runs 1–4.

the electrons are trapped into the IASW potential. These trapped electrons strongly oscillate inside the IASW potentials, which make the IASW unstable. We estimate the number of trapped electrons in the IASW potential during their evolution for all PIC simulation runs.

Trapping of charged particles in a wave potential is well known and has been reported in previous studies [*Luque and Schamel*, 2005]. *Matsumoto and Omura* [1981] have demonstrated the trapping of electron by a monochromatic wave traveling parallel to the magnetic field in inhomogeneous magnetic field. We calculate the trapping velocity $V_{\text{trap}} = 2\omega_{\text{trap}}/k$, where $\omega_{\text{trap}} = \sqrt{ekE_0/m_e}$ is the trapping frequency. Here E_0 and k respectively represent the peak amplitude of the electric field and the wave vector of IASW. We obtain the number of trapped electrons from the following equation:

$$n_{\text{trap}} = \int_{V_s - V_{\text{trap}}}^{V_s + V_{\text{trap}}} \int_{x_2}^{x_1} f_e(x, v)\, \mathrm{d}x\, \mathrm{d}v \tag{8}$$

Here wave vector $k = 2\pi/(x_1 - x_2)$. We estimate the percentage of electrons trapped by the IASW potential linked with the electron vortex traveling toward the right-side boundary of the simulation system. The V_{trap}, E_0, and percentage of the number of trapped electrons are shown respectively in Figures 7a–7c for $\Delta n = 0.05$, 0.1, 0.2, and 0.5. It is found that the percentage of trapped electrons is considerably lower for weaker IDP; however, this percentage increases with the increase in Δn of IDPs. The amplitude of the IASW potential is found to increase with the increase in amplitude of IDP. The trapping velocity is proportional to E_0; hence, the number of trapped particles is found to be higher for the IASW with larger Δn.

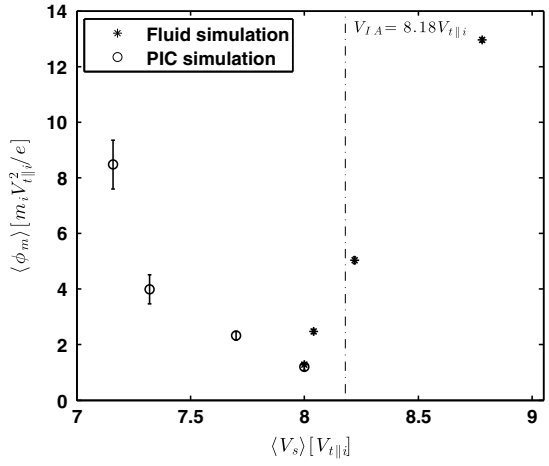

Figure 8. Average peak amplitude of IASW as a function of its phase velocity for both fluid and PIC simulations. The vertical dotted line represents the speed of IASW obtained from their linear dispersion relation, i.e., $V_{\text{IA}} = 8.18V_{t\|i}$.

4. Fluid Versus Particle-In-Cell Simulation of IASW

We summarize average properties of the IASW, namely, amplitude, speed, and width during $\omega_{pi}t$ = 40–80 for different simulation runs to compare the results from the fluid and PIC simulations. The average estimates of these properties are summarized in Table 1. These IASW characteristics are obtained from the stable propagation region before they reached the simulation boundaries. The average amplitude of IASW increases as Δn of IDP increases for both fluid and PIC simulations. However, the average amplitude of IASW linked with the electron vortices in the PIC simulations deviates considerably from those obtained from the fluid simulation for larger IDP, which is attributed to the presence of kinetic effects in the PIC simulations. For small IDP, the average amplitude and speed of IASW generated

through the fluid and PIC simulations are in close accordance. It is noticed that the average speed of IASW in the PIC simulation decreases with increase in Δn of the IDP, whereas reverse tendency is observed for IASW generated in the fluid simulation. The discrepancy in the IASW amplitude-speed relation suggests that the IASW formed in the fluid simulation show KdV-type solitary wave behavior, whereas in the PIC simulation they show non-KdV-type solitary wave behavior [*Remoissenet*, 1999]. Figure 8 shows the average peak amplitude of IASW as a function of its average speed for the fluid and PIC simulations. The vertical dotted line corresponds to the IASW speed obtained from their linear dispersion relation (V_{IA}). It is noticed that for $V_s < V_{IA}$, the characteristics of IASW from the fluid simulation are in close agreement with those obtained from the PIC simulation and they are associated with the IDP with less than 15% perturbations. For density perturbations greater than 15%, the V_s exceeds V_{IA} and the IASW characteristics obtained from the fluid and PIC simulations are considerably different. For the IASW with V_s less than V_{IA}, both fluid and kinetic approaches can be used to model satellite observations of the IASW. However, when $V_s > V_{IA}$, use of the kinetic treatment is appropriate to model the IASW observations.

Kakad et al. [2013] have shown that the electrostatic energy and the kinetic energy of electrons increase with increase of amplitude of IDP. The enhanced kinetic energy of electrons assists to maintain the higher velocity when the amplitude of the IASW is increased. However, in the PIC simulation the scenario is different due to trapping of electrons in the IASW potentials. The number of trapped particles increases with the IASW amplitude. As a larger number of particles is trapped inside the IASW potential, it becomes more massive and moves with slower phase velocity in order to conserve its momentum.

5. Discussion and Conclusions

We have performed one-dimensional fluid and PIC simulations to study macroscale and microscale dynamical behavior of the IASW in the plasma. The fluid simulation shows stable propagation of the ion acoustic solitary structures, while in the case of the PIC simulation, their propagation characteristics are found to be influenced by the number of trapped electrons inside the IASW potentials. It is noted that the trapped electron population increases with the increase of IDP Δn in plasma. The characteristics of the IASW obtained from the PIC simulations are in close agreement with those obtained from the fluid simulations for weak IDPs, whereas the IASW generated due to strong IDPs in the PIC simulation vary significantly from those generated in the fluid simulations. The observed discrepancy in the characteristics of the IASW for the PIC and fluid simulations is attributed to the trapping of electrons in the IASW potentials, which is not considered in the fluid simulations. IASWs are low-frequency waves, in which the restoring force comes from the thermal pressure of electrons, whereas the ion mass provides the driving force to maintain the wave. In this paper, both fluid and PIC simulations use the standard initial perturbation in the equilibrium electron and ion densities, which evolves into the IASW and Langmuir waves. This is one possible way of triggering IASW, and such density perturbations can originate in the Earth's magnetospheric regions, such as bow shock, magnetopause, and magnetosheath driven by solar wind variations [*Sibeck and Gosling*, 1996].

Since the ion-acoustic mode is nondispersive, the several Fourier components that make up the IASW propagate without distortion in both fluid and kinetic models. In contrast, the Langmuir waves are highly dispersive and different Fourier components propagate with different damping rates by the Landau process in the kinetic model, but not in the fluid model. Thus, the Langmuir waves appear differently in the two models and also they decay spatially in the PIC model. In the PIC simulations the positive potentials associated with the IASW attract the electrons, which then gets trapped inside these potentials, and high dense electron islands are formed in the plasma. These structures appear as rotating vortices of trapped electrons in phase space. The trapped electrons oscillate inside the electrostatic potentials and get accelerated by the IASW. It is well known that the electron holes are positive potential perturbations, which trap the electrons in their potentials. The PIC simulation shows that even the IASW has a positive potential that traps electrons in it. Though both electron holes and IASW are linked with positive potential and electron trapping process, they posses different characteristics. In electron holes the density of trapped particles is lower than the density of free and reflected particles. They require two electron (cold and hot) components for their formation in plasma. However, our PIC simulations show that the IASW is associated with the island of trapped electrons, in which the population of trapped electrons is greater than the density of free and reflected particles. They require electron temperature higher than ion temperature for their formation. The speed of the IASW in the fluid simulations increases with the increase of the IASW amplitude, which demonstrates that they are KdV-type solitary waves. In the PIC simulation, the IASW speed is found to decrease

with the increase of the IASW amplitude, which indicates that they are non-KdV-type solitary waves [*Remoissenet*, 1999].

The multispecies plasma fluid models are renowned and have been extensively used in the study of electrostatic solitary waves in terms of electron and ion acoustic solitary waves. *Berthomier et al.* [1998] used the nonlinear multifluid model consisting of cold electrons, hot electrons, and ions to model the IASW characteristics observed by the Viking satellite in the auroral region of the Earth's magnetosphere. The IASW with both positive and negative potentials are observed in this region [*Lotko and Kennel*, 1983; *Temerin et al.*, 1982]. The bipolar electric field pulses with the amplitude range of 20–40 mV/m associated with the IASW and observed by the Viking were explained by *Berthomier et al.* [1998]. This electric field amplitude corresponds to 0.13–0.3 in the units of $m_i\omega_{pi}V_{t\|i}/e$. In their study, the observed hot electron to ion temperature ratio, $T_e/T_i = 40$ was considered to model the observed IASW structures. In the present simulation, only hot electrons and ions with temperature ratio, $T_e/T_i = 64$ are assumed for all the simulation runs. The electric field obtained in the simulation is found to be of the order of 0.05–0.3 $m_i\omega_{pi}V_{t\|i}/e$, which is in agreement with the Viking observations. However, the polarity of the electric field pulses in the simulations is opposite to that of electric field pulses observed by the Viking. It should be noted that exact comparison between simulations and data is difficult because wave propagation directions relative to the spacecraft cannot be unambiguously determined from single-spacecraft measurement such as Viking [*Temerin et al.*, 1982]. Furthermore, we would like to point out that the observed electric field pulses are associated with density depletions, whereas they are associated with the density humps in the present simulations. This could be due to the presence of an additional cold electron component in the auroral region. The model with hot electrons and ions with $T_e > T_i$ supports only positive amplitude IASWs, and they are associated with positive density humps [*Kakad et al.*, 2013], which is consistent with results from the present simulations.

We have tested the validity of our fluid code as a nonlinear physical model [*Kakad et al.*, 2013]. The fluid simulations successfully validated the nonlinear fluid theory [*Sagdeev*, 1966], which is extensively used to model electrostatic solitary wave observations in space plasmas. The use of different numerical schemes in the simulations should not affect the results. In this respect, it is clear that our fluid model can study the nonlinear physics correctly. The PIC and fluid simulations performed in the present study suggest that the IASW triggered by small perturbations can be explained by either fluid or kinetic approach. However, for the IASW generated due to large perturbations, the numbers of trapped electrons in the IASW potential are significant. The resonant interaction of IASW with the bounce motion of trapped electrons affects the dynamics of the IASW. Thus, the use of the fluid treatment in such a case is not appropriate and it is necessary to consider the kinetic approach in the solitary wave models/simulations for better understanding and interpretation of satellite observations of the IASW in space plasmas.

Acknowledgments

The simulation runs were performed with supercomputer facilities at Research Institute for Sustainable Humanosphere and Academic Center for Computing and Media Studies of Kyoto University. This work is supported by grant-in-aid 23.01024 for JSPS fellows and 26287120 of the Ministry of Culture, Sports, Science, and Technology in Japan.

Larry Kepko thanks Nagendra Singh and another reviewer for their assistance in evaluating the paper.

References

Bale, S. D., P. J. Kellogg, D. E. Larsen, R. P. Lin, K. Goetz, and R. P. Lepping (1998), Bipolar electrostatic structures in the shock transition region: Evidence of electron phase space holes, *Geophys. Res. Lett.*, *25*(15), 2929–2932, doi:10.1029/98GL02111.

Baluku, T. K., M. A. Hellberg, and F. Verheest (2010), New light on ion acoustic solitary waves in a plasma with two-temperature electrons, *Europhys. Lett.*, *91*(1), 15001, doi:10.1209/0295-5075/91/15001.

Bernstein, I. B., J. M. Greene, and M. D. Kruskal (1957), Exact nonlinear plasma oscillations, *Phys. Rev.*, *108*(3), 546–550, doi:10.1103/PhysRev.108.546.

Berthomier, M., R. Pottelette, and M. Malingre (1998), Solitary waves and weak double layers in a two-electron temperature auroral plasma, *J. Geophys. Res.*, *103*(A3), 4261–4270, doi:10.1029/97JA00338.

Dubouloz, N., R. A. Treumann, R. Pottelette, and M. Malingre (1993), Turbulence generated by a gas of electron acoustic solitons, *J. Geophys. Res.*, *98*(A10), 17,415–17,422, doi:10.1029/93JA01611.

Ergun, R. E., et al. (1998), Fast satellite observations of large-amplitude solitary structures, *Geophys. Res. Lett.*, *25*(12), 2041–2044, doi:10.1029/98GL00636.

Franz, J. R., P. M. Kintner, and J. S. Pickett (1998), Polar observations of coherent electric field structures, *Geophys. Res. Lett.*, *25*(8), 1277–1280, doi:10.1029/98GL50870.

Ghosh, S. S., J. S. Pickett, G. S. Lakhina, J. D. Winningham, B. Lavraud, and P. M. E. Décréau (2008), Parametric analysis of positive amplitude electron acoustic solitary waves in a magnetized plasma and its application to boundary layers, *J. Geophys. Res.*, *113*, A06218, doi:10.1029/2007JA012768.

Goldman, M. V., M. M. Oppenheim, and D. L. Newman (1999), Nonlinear two-stream instabilities as an explanation for auroral bipolar wave structures, *Geophys. Res. Lett.*, *26*(13), 1821–1824, doi:10.1029/1999GL900435.

Kakad, A., Y. Omura, and B. Kakad (2013), Experimental evidence of ion acoustic soliton chain formation and validation of nonlinear fluid theory, *Phys. Plasmas*, *20*(6), 062103, doi:10.1063/1.4810794.

Kakad, A. P., S. V. Singh, R. V. Reddy, G. S. Lakhina, S. G. Tagare, and F. Verheest (2007), Generation mechanism for electron acoustic solitary waves, *Phys. Plasmas*, *14*(5), 052305, doi:10.1063/1.2732176.

Kakad, A. P., S. V. Singh, R. V. Reddy, G. S. Lakhina, and S. G. Tagare (2009), Electron acoustic solitary waves in the Earth's magnetotail region, *Adv. Space Res.*, *43*(12), 1945–1949, doi:10.1016/j.asr.2009.03.005.

Lakhina, G. S., A. P. Kakad, S. V. Singh, and F. Verheest (2008a), Ion- and electron-acoustic solitons in two-electron temperature space plasmas, *Phys. Plasmas*, *15*(6), 062903, doi:10.1063/1.2930469.

Lakhina, G. S., S. V. Singh, A. P. Kakad, F. Verheest, and R. Bharuthram (2008b), Study of nonlinear ion- and electron-acoustic waves in multi-component space plasmas, *Nonlinear Processes Geophys.*, *15*(6), 903–913, doi:10.5194/npg-15-903-2008.

Lakhina, G. S., S. V. Singh, A. P. Kakad, M. L. Goldstein, A. F. Viñas, and J. S. Picket (2009), A mechanism for electrostatic solitary structures in the Earth's magnetosheath, *J. Geophys. Res.*, *114*(9), A09212, doi:10.1029/2009JA014306.

Lakhina, G. S., S. V. Singh, and A. P. Kakad (2011a), Ion- and electron-acoustic solitons and double layers in multi-component space plasmas, *Adv. Space Res.*, *47*(9), 1558–1567, doi:10.1016/j.asr.2010.12.013.

Lakhina, G. S., S. V. Singh, A. P. Kakad, and J. S. Pickett (2011b), Generation of electrostatic solitary waves in the plasma sheet boundary layer, *J. Geophys. Res.*, *116*, A10218, doi:10.1029/2011JA016700.

Lotko, W., and C. F. Kennel (1983), Spiky ion acoustic waves in collisionless auroral plasma, *J. Geophys. Res.*, *88*(A1), 381–394, doi:10.1029/JA088iA01p00381.

Luque, A., and H. Schamel (2005), Electrostatic trapping as a key to the dynamics of plasmas, fluids and other collective systems, *Phys. Rep.*, *415*(5–6), 261–359, doi:10.1016/j.physrep.2005.05.002.

Matsumoto, H., and Y. Omura (1981), Cluster and channel effect phase bunchings by whistler waves in the nonuniform geomagnetic field, *J. Geophys. Res.*, *86*(A2), 779–791, doi:10.1029/JA086iA02p00779.

Matsumoto, H., H. Kojima, T. Miyatake, Y. Omura, M. Okada, I. Nagano, and M. Tsutui (1994), Electrostatic solitary waves (ESW) in the magnetotail: BEN wave forms observed by GEOTAIL, *Geophys. Res. Lett.*, *21*(25), 2915–2918, doi:10.1029/94GL01284.

Omura, Y. (2007), One-dimensional electromagnetic particle code KEMPO1: A tutorial on microphysics in space plasmas, in *Advanced Methods for Space Simulations*, edited by H. Usui and Y. Omura, pp. 1–21, Terra Scientific Publishing Company, Tokyo, Japan.

Omura, Y., and H. Matsumoto (1993), KEMPO1: Technical guide to one-dimensional electromagnetic particle code, in *Computer Space Plasma Physics: Simulation Techniques and Software*, edited by H. Matsumoto and Y. Omura, pp. 21–65, Terra Scientific Publishing Company, Tokyo, Japan.

Omura, Y., H. Kojima, and H. Matsumoto (1994), Computer simulation of electrostatic solitary waves: A nonlinear model of broadband electrostatic noise, *Geophys. Res. Lett.*, *21*(25), 2923–2926, doi:10.1029/94GL01605.

Omura, Y., H. Matsumoto, T. Miyake, and H. Kojima (1996), Electron beam instabilities as generation mechanism of electrostatic solitary waves in the magnetotail, *J. Geophys. Res.*, *101*(A2), 2685–2697, doi:10.1029/95JA03145.

Pickett, J. S., et al. (2004), Solitary waves observed in the auroral zone: The cluster multi-spacecraft perspective, *Nonlinear Processes Geophys.*, *11*(2), 183–196, doi:10.5194/npg-11-183-2004.

Remoissenet, M. (1999), *Waves Called Solitons: Concepts and Experiments*, 44–45, 3rd ed., Springer-Verlag, New York.

Sagdeev, R. Z. (1966), Cooperative phenomena and shock waves in collisionless plasmas, in *Reviews of Plasma Physics*, vol. 4, edited by M. Leontovich, pp. 23–91, Consultants Bureau, New York.

Sibeck, D. G., and J. T. Gosling (1996), Cluster and channel effect phase bunchings by whistler waves in the nonuniform geomagnetic field, *J. Geophys. Res.*, *101*(A1), 31–40, doi:10.1029/95JA03141.

Singh, N. (1973), High-Mach number electrostatic shocks in collisionless plasmas, *J. Pure Appl. Phys.*, *11*, 533–534.

Singh, N., and G. Khazanov (2003), Double layers in expanding plasmas and their relevance to the auroral plasma processes, *J. Geophys. Res.*, *108*(A4), 8007, doi:10.1029/2002JA009436.

Singh, S. V., R. V. Reddy, and G. S. Lakhina (2001), Broadband electrostatic noise due to nonlinear electron-acoustic waves, *Adv. Space Res.*, *28*(11), 1643–1648, doi:10.1016/S0273-1177(01)00479-3.

Temerin, M., K. Cerny, W. Lotko, and F. S. Mozer (1982), Observations of double layers and solitary waves in the auroral plasma, *Phys. Rev. Lett.*, *48*(17), 1175–1178, doi:10.1103/PhysRevLett.48.1175.

Verheest, F., M. A. Hellberg, and I. Kourakis (2013), Electrostatic supersolitons in three-species plasmas, *Phys. Plasmas*, *20*(1), 012302, doi:10.1063/1.4775085.

Washimi, H., and T. Taniuti (1966), Propagation of ion-acoustic solitary waves of small amplitude, *Phys. Rev. Lett.*, *17*(19), 996–998, doi:10.1103/PhysRevLett.17.996.